



Interpretation of Radio Wave Scintillation Observed through LOFAR Radio Telescopes

Biagio Forte¹ , Richard A. Fallows^{2,3} , Mario M. Bisi³ , Jinge Zhang⁴ , Andrzej Krankowski⁵ , Bartosz Dabrowski⁵ ,
Hanna Rothkaehl⁶ , and Christian Vocks⁷

¹ Department of Electronic and Electrical Engineering, University of Bath, UK; B.Forte@bath.ac.uk

² ASTRON, Oude Hoogeveensedijk 4, 7991 PD Dwingeloo, The Netherlands

³ RAL Space, United Kingdom Research and Innovation (UKRI) – Science & Technology Facilities Council (STFC) – Rutherford Appleton Laboratory (RAL), Harwell Campus, Oxfordshire, OX11 0QX, UK

⁴ Mullard Space Science Laboratory, University College London, UK

⁵ Space Radio-Diagnostics Research Centre, University of Warmia and Mazury in Olsztyn, Poland

⁶ Space Research Centre, Polish Academy of Sciences, Bartycka 18A, 00-716 Warsaw, Poland

⁷ Leibniz-Institut für Astrophysik Potsdam (AIP), Potsdam, Germany

Received 2021 April 16; revised 2022 April 14; accepted 2022 May 2; published 2022 December 6

Abstract

Radio waves propagating through a medium containing irregularities in the spatial distribution of the electron density develop fluctuations in their intensities and phases. In the case of radio waves emitted from astronomical objects, they propagate through electron density irregularities in the interstellar medium, the interplanetary medium, and Earth's ionosphere. The LOFAR radio telescope, with stations across Europe, can measure intensity across the VHF radio band and thus intensity scintillation on the signals received from compact astronomical objects. Modeling intensity scintillation allows the estimate of various parameters of the propagation medium, for example, its drift velocity and its turbulent power spectrum. However, these estimates are based on the assumptions of ergodicity of the observed intensity fluctuations and, typically, of weak scattering. A case study of single-station LOFAR observations of the strong astronomical source Cassiopeia A in the VHF range is utilized to illustrate deviations from ergodicity, as well as the presence of both weak and strong scattering. Here it is demonstrated how these aspects can lead to misleading estimates of the propagation medium properties, for example, in the solar wind. This analysis provides a method to model errors in these estimates, which can be used in the characterization of both the interplanetary medium and Earth's ionosphere. Although the discussion is limited to the case of the interplanetary medium and Earth's ionosphere, its ideas are also applicable to the case of the interstellar medium.

Unified Astronomy Thesaurus concepts: [Interplanetary scintillation \(828\)](#); [Ionospheric scintillation \(861\)](#); [Radio telescopes \(1360\)](#)

1. Introduction

The propagation of radio waves through a medium containing inhomogeneities in the spatial distribution of the refractive index causes distortion in the radio wave front. These changes in phase across the wave front then develop into fluctuations in the intensity of the radio waves as the propagation distance increases. If the inhomogeneities in the refractive index drift across the ray path, then a time-varying interference-like pattern is observed at the receiver. The time-varying interference pattern consists of temporal fluctuations in the intensity and phase of the received wave as a result of phase changes induced by refractive index irregularities in a scattering-like mechanism. This temporal fluctuation in the intensity and phase of the received radio waves is known as radio wave scintillation. In the case of electromagnetic waves in VHF, UHF, L, C, and S bands received from astronomical radio sources, refractive index inhomogeneities are due to irregularities occurring in the spatial distribution of the electron density in magnetized plasmas such as Earth's ionosphere, the interplanetary medium, and the interstellar medium.

The problem of scintillation originating from the propagation of radio waves through plasma inhomogeneities in Earth's ionosphere and in the interplanetary medium was studied

initially in radio astronomy as early as the 1950s (Ratcliffe 1956; Mercier 1962; Briggs & Parkin 1963; Hewish et al. 1964; Little & Hewish 1966; Salpeter 1967). Later, with the advent of artificial satellites, ionospheric scintillation has been widely observed, measured, and studied by using satellite signals. Beacons on geostationary satellites, geostationary links for telecommunications, and multifrequency polar-orbiting satellites were used to carry out the first measurements and characterization of ionospheric scintillation using frequencies from 40 MHz up to C band (Fremouw et al. 1978; Vats et al. 1981; Basu et al. 1988; Secan et al. 1997). More recently, the main source of information is provided by signals from Global Navigation Satellite Systems (GNSS), which utilize radio waves in the L band (Skone et al. 2001; Jiao et al. 2013; Alfonsi et al. 2013; Chermiak et al. 2018; Zakharenkova et al. 2019; Kotulak et al. 2020).

When observing radio waves emitted from astronomical radio sources, it is plausible to assume that scintillation can originate from electron density irregularities either in Earth's ionosphere, in the solar wind (interplanetary medium), outside the solar system (interstellar medium), or from a combination of them. In the case of Earth's ionosphere radio wave scintillation is experienced during trans-ionospheric propagation (for radio waves frequencies in VHF, UHF, L, S, C bands) through irregularities in the electron density spatial distribution (Aarons 1982; Yeh & Liu 1982) that form in the ionosphere as a consequence of plasma instabilities, such as the Rayleigh–Taylor and the Kelvin–Helmholtz instabilities in the auroral,



Original content from this work may be used under the terms of the [Creative Commons Attribution 4.0 licence](#). Any further distribution of this work must maintain attribution to the author(s) and the title of the work, journal citation and DOI.

polar, and equatorial ionosphere, or the Perkins instability in the middle latitudes (Kelley 2009). In the case of the interplanetary medium, irregularities form as a consequence of the solar wind and travel with the solar wind under frozen-in conditions (Briggs & Parkin 1963; Hewish et al. 1964; Salpeter 1967; Redhead 1971). The same assumption is made for irregularities in the interstellar medium (Stinebring et al. 2001; Stinebring 2006).

Scintillation can be seen as the manifestation of the scattering of the radio waves energy when propagating through electron density irregularities. Such a scattering can be weak (low scintillation) or strong (high scintillation). The former can be well described through a diffractive scattering mechanism (typically approximated by means of propagation through a single phase-changing screen), whereas the latter requires a mechanism based on multiple and refractive scattering (typically approximated by propagation through many phase-changing screens in an extended medium).

The work presented here addresses the problem of scintillation occurring simultaneously on a number of radio wave frequencies in the VHF band emitted from astronomical sources and measured on Earth through, e.g., the Kilpisjärvi Atmospheric Imaging Receiver Array (KAIRA; Fallows et al. 2014; McKay-Bukowski et al. 2015) or the Low Frequency Array (LOFAR; van Haarlem et al. 2013; Fallows et al. 2020) radio facilities.

An example data set covering the frequency range 29–64 MHz and recorded by LOFAR is considered here and used to observe how scintillation and the scattering regime change with frequency in response to the same spatial distribution of electron density irregularities and their energy cascade.

The wide interval of frequencies that can be simultaneously observed through LOFAR enables the characterization of ionospheric irregularities and instability mechanisms in the ionosphere in a more comprehensive fashion than through the use of radio waves transmitted from artificial satellites, typically with only two, or very few, frequencies available.

The main theoretical aspects in the modeling of radio waves scintillation are briefly reviewed here. Then, a case study of a single-station LOFAR observation of radio wave scintillation is presented to discuss how these observations can be modeled and how parameters related to the propagation medium can be inferred. In particular, the implications of the assumption of ergodicity and weak scattering in the experimental observations are investigated in order to model corresponding errors.

2. The Problem of Radio Wave Scintillation

Before considering the LOFAR observation in detail, it is helpful to state the problem of radio wave scintillation and to review the main results that can be used for the interpretation of experimental observations. The main treatment and results are contained in Yeh & Liu (1982), Ishimaru (1978), and Uscinski (1977). A notation similar to the description utilized in these references is adopted here to facilitate the reader.

Assume that an electromagnetic wave is transmitted from a pointlike radio source and propagates along z to a receiver located at z_R . During its propagation, it encounters a region with electron density irregularities where scintillation originates following weak or multiple scattering. By adopting a coordinate system such that z is the propagation direction and assuming a monochromatic plane wave where the electric field

has only one component, the wave incident on the medium with ionized irregularities can be written as (Yeh & Liu 1982)

$$E(x, y, z, \omega, t) = U(x, y, z, \omega, t) e^{-jkz} e^{j\omega t}, \quad (1)$$

where $U(x, y, z, \omega, t)$ is the complex amplitude of the electric field component $E(x, y, z, \omega, t)$ at point (x, y, z) with angular frequency ω .

The electric field amplitude received at the point (x_R, y_R, z_R) after propagation through a phase-changing medium can be written (by utilizing a notation similar to Yeh & Liu 1982) in the form (Yeh & Liu 1982; Ishimaru 1978)

$$U(x_R, y_R, z_R, \omega, t) = U_0 e^{\psi(x_R, y_R, z_R, \omega, t)}, \quad (2)$$

where U_0 is the amplitude of the incident wave and

$$\begin{aligned} \psi(x_R, y_R, z_R, \omega, t) = & \chi(x_R, y_R, z_R, \omega, t) \\ & - jS(x_R, y_R, z_R, \omega, t), \end{aligned} \quad (3)$$

where χ is the log-amplitude and S the phase of the received fluctuations in the signal. An iterative series solution can be developed for ψ (Rytov solution; Yeh & Liu 1982; Ishimaru 1978).

The propagation through a medium containing electron density irregularities can be approximated by assuming (Figure 1) that the radio waves propagate through an infinitesimally thin phase-changing screen or through a phase screen of finite thickness L (Mercier 1962; Salpeter 1967). The phase perturbations imposed on the wave front then transform into amplitude fluctuations as the propagation distance increases (Uscinski 1977).

In the case of weak scattering it is assumed that (a) the wavelength is much smaller than the typical size of the electron density irregularities in the screen and (b) the phase change introduced by the screen is always very small. Under these assumptions, it can be shown that the power spectral densities for the log-amplitude χ and the phase S received at (x_R, y_R, z_R) can be described through (Salpeter 1967; Yeh & Liu 1982)

$$\begin{aligned} \Phi_\chi(\nu) \sim & \frac{\pi r_e^2 \lambda^2 L}{V^{\text{REL}}} \int_{-\infty}^{+\infty} \\ & \times \left\{ 1 \mp \frac{\sin \left[\frac{\kappa^2 L}{2k} \right]}{\frac{\kappa^2 L}{2k}} \cos \left[\frac{\kappa^2}{k} \left(z_R - \frac{L}{2} \right) \right] \right\} \\ & \times \Phi_{\Delta N} \left(\frac{2\pi\nu}{V^{\text{REL}}}, \kappa_y, 0 \right) d\kappa_y, \end{aligned} \quad (4)$$

where ν is the temporal frequency (in hertz), λ is the wavelength, k is the angular wavenumber, V^{REL} is the relative velocity between the ray path and the screen in the x -direction, r_e is the classical electron radius, and

$$\kappa^2 = \frac{(2\pi)^2 \nu^2}{(V^{\text{REL}})^2} + \kappa_y^2. \quad (5)$$

The function $\Phi_{\Delta N} \left(\frac{2\pi\nu}{V^{\text{REL}}}, \kappa_y, 0 \right)$ represents the spatial power spectral density of the electron density irregularities within a two-dimensional screen that drifts across the ray path along the x -direction only. The transformation from spatial to temporal frequencies in Equations (4)–(5) follows from the assumption

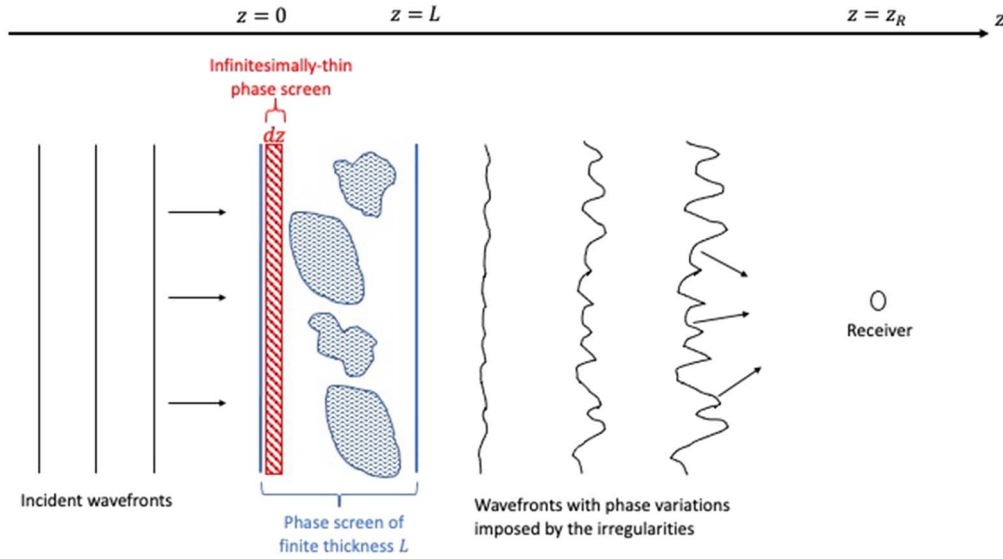


Figure 1. The geometry of the propagation problem with reference to the case of an infinitesimally thin phase screen and to the case of an extended phase screen.

that (Ishimaru 1978)

$$\Delta N(x, y, z, t) = \Delta N(x - V^{\text{REL}}t, y, z, 0), \quad (6)$$

where the electron density irregularities are characterized through the function $\Delta N(x, y, z, t)$, which is the difference between the electron density $N(x, y, z, t)$ and its background average. Equation (6) considers electron density irregularities as frozen-in while traversing the ray path.

The spatial filtering function within curly brackets in Equation (4) has the first maximum at

$$\kappa_F = \frac{2\pi}{\sqrt{2\lambda z_R}}, \quad (7)$$

where it is assumed that $\kappa_y = 0$ in the case of a 1D phase screen. Equation (7) applies both in the limit of an extended medium with $z_R = L$ (Ishimaru 1978) and in the limit of an infinitesimally thin screen with $L \rightarrow 0$ (Yeh & Liu 1982). The scale $d_F = \sqrt{2\lambda z_R}$ is the Fresnel scale, and the temporal Fresnel frequency is given by

$$\nu_F = \frac{V^{\text{REL}}}{\sqrt{2\lambda z_R}}. \quad (8)$$

The spectral form in Equation (4) can be expanded to include additional filtering functions that describe the presence of an extended source (Hewish et al. 1964; Little & Hewish 1966; Budden & Uscinski 1970), as well as, in the case of scattering due to the interplanetary medium, the distance between the ray path and the Sun (i.e., elongation of the source; Manoharan & Ananthakrishnan 1990; Ishimaru 1978). The effect of the source filtering function, for example, is that of a low-pass filtering (Little & Hewish 1966; Manoharan & Ananthakrishnan 1990; Yamauchi et al. 1996).

The intensity of the radio wave is given by

$$I(x, y, z, \omega, t) = U(x, y, z, \omega, t)U^*(x, y, z, \omega, t), \quad (9)$$

where $U^*(x, y, z, \omega, t)$ is the complex conjugate of $U(x, y, z, \omega, t)$.

At the receiver position (x_R, y_R, z_R) the amount of scintillation originating from electron density irregularities along the ray path can be quantified by estimating the intensity fluctuations observed through the scintillation index (Briggs & Parkin 1963):

$$S_4^2 = \frac{\langle I^2 \rangle - \langle I \rangle^2}{\langle I \rangle^2}, \quad (10)$$

where $\langle \rangle$ denotes ensemble averaging.

In the weak scattering approximation it can be shown that the power spectral density for the intensity $\Phi_I(\nu)$ has a similar shape to $\Phi_\chi(\nu)$ described in Equation (4), using the first-order approximation as follows (Uscinski 1977):

$$I(x, y, z, \omega, t) \approx 1 + 2\chi(x, y, z, \omega, t). \quad (11)$$

For a turbulent screen (Yeh & Liu 1982) the spectrum of irregularities is

$$\Phi_{\Delta N} \sim \kappa_x^{-p} \quad (12)$$

in the inertial subrange between an outer scale L_0 and an inner scale l_0 .

In the case of weak scattering and in the presence of $\Phi_{\Delta N}$ given in Equation (12), the temporal spectrum $\Phi_I(\nu)$ asymptotically follows a power law of $1 - p$ for $\nu > \nu_F$, while it is asymptotically constant for $\nu < \nu_F$ as a result of Equations (4) and (12) (Yeh & Liu 1982). It follows that electron density irregularities with scales smaller than the Fresnel scale mainly contribute to intensity fluctuations, while the contribution from irregularities with scales larger than the Fresnel scale is largely filtered out (Yeh & Liu 1982).

It is worth noting that various definitions of the Fresnel frequency can be found in the literature. The definitions follow from particular values of the spatial filtering function that characterize the power spectral density of the intensity fluctuations. For example, Manoharan & Ananthakrishnan (1990) adopted a definition for the Fresnel scale based on the spatial filtering function within $\Phi_I(\nu)$ derived in Salpeter (1967), which assumed a one-dimensional (infinitesimally) thin screen. In this case it is defined as $\kappa_F \approx \sqrt{4\pi/\lambda z_R}$ (Salpeter 1967; Manoharan & Ananthakrishnan 1990; Yamauchi et al. 1996), which corresponds

to the argument of the filtering function being equal to 1 (Equation (4)). On the other hand, Yeh & Liu (1982) and Ishimaru (1978) described the more general case of a two-dimensional extended screen: Yeh & Liu (1982) considered a phase screen of finite thickness L between $z = 0$ and $z = L$, while Ishimaru (1978) assumed an extended medium between $z = 0$ and $z = z_R$. In both cases, through the Rytov solution for weak scattering, the spatial filtering function within $\Phi_\chi(\nu)$ leads to a spatial Fresnel frequency of $\kappa_F = 2\pi/\sqrt{2\lambda z_R}$, which corresponds to the first maximum of the filtering function (the two definitions are numerically similar). The definition of $\kappa_F = 2\pi/\sqrt{2\lambda z_R}$ also applies to the case of an infinitesimally thin phase screen in the limit of $L \rightarrow 0$. In view of Equations (4), (11), and (12), and on the basis of the asymptotic behavior for $\Phi_I(\nu)$ for a two-dimensional turbulent screen, the definition for the Fresnel frequency in Equation (8) is given in accordance with the same definition adopted in Yeh & Liu (1982) and Ishimaru (1978).

The results of the weak scattering approximation are based on the assumption of a single phase screen. Under this approximation, the phase change introduced by the screen (also known as single weak scattering) is assumed to be very small, and intensity fluctuations are produced as the propagation distance increases: this mechanism is known as the distance effect. This approximation tends to be more accurate in the presence of lower values of the scintillation index S_4 .

In the presence of higher and/or saturating values of the scintillation index S_4 , intensity fluctuations can be produced by multiple scattering from many irregularities within an extended medium in combination with the distance effect. The total phase change introduced by multiple scattering is higher (i.e., strong scattering) than in the single weak scattering case.

In the presence of (single) weak scattering, intensity fluctuations are fully developed when $z > \sqrt{2\lambda z_R}$ (the Fraunhofer region), and the intensity scintillation approaches asymptotically the value $S_4^2 \xrightarrow{z \rightarrow \infty} 2\sigma_S^2 \sim 2k^2L$, where σ_S is the standard deviation of the phase fluctuation (Uscinski 1977; Ishimaru 1978), which is determined by the phase change introduced by the screen. On the other hand, in the presence of strong scattering the asymptotic limit of S_4^2 (which includes cases of higher and saturating S_4 values) is determined by the combination of strong scattering and the distance effect (Uscinski 1977).

In the presence of strong scattering, spectral broadening is observed for $\Phi_I(\nu)$, where the roll-off at higher temporal frequencies is no longer given by a power law but by a steeper Gaussian law when strong scattering is fully developed. In this case, radio waves can be described by means of focusing and defocusing rays, where the focal distance typically varies with the amount of multiple scattering (Uscinski 1977; Booker & Majidihi 1981).

When the intensity of radio waves can be measured simultaneously over several frequencies, as in the case of the LOFAR radio telescope, the two-frequency two-time correlation function of the received intensity at the receiving point (x_R, y_R, z_R) can be written as (Ishimaru 1978)

$$B_I(x_R, y_R, z_R, \omega_d, \tau) = \langle I(x_R, y_R, z_R, \omega_1, t_1) I(x_R, y_R, z_R, \omega_2, t_2) \rangle, \quad (13)$$

where $\omega_d = \omega_1 - \omega_2$ and $\tau = t_1 - t_2$. The two-dimensional Fourier transform of B_I over ω_d and τ gives the two-dimensional power spectral density $P_I(t_d, f_D)$ of the intensity

(Jokipii 1973; Uscinski 1977; Knepp 1983; Ishimaru 1978):

$$P_I(t_d, f_D) = \int_{-\infty}^{+\infty} \int_{-\infty}^{+\infty} B_I(x_R, y_R, z_R, \omega_d, \tau) \times e^{-j(\omega_d t_d + 2\pi f_D \tau)} d\omega_d d\tau. \quad (14)$$

The spread in the time delay t_d between multiple ray paths and in the Doppler frequency f_D due to the relative motion between ray paths and electron density irregularities can be used to infer the amount of scattering, the scales involved in the scattering, and their dynamics (Knepp & Nickisch 2009; Fallows et al. 2014, 2020).

The power spectral density $P_I(t_d, f_D)$ has been labeled in the recent ionospheric scintillation literature as the generalized spectrum, and in the radio astronomy literature as the secondary spectrum, or the delay-Doppler function (Yeh & Liu 1982; Knepp 1983). However, while in pulse propagation the generalized spectrum is considered as the Fourier transform of the amplitude correlation function (i.e., the second-order moment or mutual coherence function; Bello 1963; Knepp 1983; Nickisch 1992; Lambert & Rickett 1999), in recent radio astronomy the generalized spectrum has been considered in Equation (14) as the Fourier transform of the intensity correlation function (i.e., the fourth-order moment; Stinebring et al. 2001; Walker et al. 2004; Cordes et al. 2006; Stinebring 2006; Fallows et al. 2014). In the presence of weak scattering, the two spectra are proportional (apart from an additive constant), as it can be shown that (Uscinski 1977)

$$B_I(x_R, y_R, z_R, \omega_d, \tau) \sim \langle \chi(x_R, y_R, z_R, \omega_1, t_1) \chi(x_R, y_R, z_R, \omega_2, t_2) \rangle, \quad (15)$$

whereas in the presence of strong scattering the two spectra are related through convolution in the limit of points separated by an infinite distance (Ishimaru 1978).

An important aspect needs to be noted here. The lack of precise knowledge of the functional form describing the spatial distribution of the electron density irregularities ΔN prevents a deterministic solution to the propagation problem. Thus, the treatment of the scintillation problem assumes that the fluctuations ΔN in the electron density distribution $N(x, y, z, t)$ are a homogeneous (stationary) random function. This follows from the concept that the difference function

$$\Delta N(x, y, z, t) = N(x, y, z, t) - \langle N \rangle \quad (16)$$

is assumed to be a homogeneous (stationary) random function even if the function $N(x, y, z, t)$ is not (Uscinski 1977; Ishimaru 1978). In Equation (16) $\langle N \rangle$ represents the background average of the electron density. In turn, the fluctuations of the amplitude, intensity, and phase of the radio wave originating from ΔN are considered to be stationary random functions. Hence, the statistical solution of the problem is based on the ensemble average of an infinite number of realizations of a homogeneous stationary random function, where each realization follows the same probability density function (Uscinski 1977; Ishimaru 1978).

In practice, experimental observations measure the intensity of a radio wave at a single point as a function of time. Temporal averaging is utilized instead of ensemble averaging; that is, an implicit assumption of ergodicity is made on the basis that the temporal resolution of the receiver averages over a large enough number of realizations within the ensemble

(Uscinski 1977). The assumption of ergodicity can be justified if the propagation time through the irregularities is much shorter than the temporal scale over which the irregularities in the medium evolve and if the temporal resolution of the receiver is much longer than the propagation time through the irregularities and much shorter than the temporal evolution of irregularities.

In the case of LOFAR observations two important questions arise: (1) whether the assumption of ergodicity is verified and how properties of the irregularities can be inferred throughout different scattering regimes, and (2) whether it is possible to distinguish, within data recorded by a single station, between scintillation originating from Earth's ionosphere, the interplanetary medium, and the interstellar medium.

3. Verification of Ergodicity

The problem of ergodicity (i.e., question (1)) is related to the capability of recognizing whether the intensity fluctuations originated from a phase screen drifting across the ray path (with a drifting velocity) or whether they originated from temporal changes in the propagation medium that occur when the temporal resolution of the receiver is longer than the temporal evolution of the irregularities.

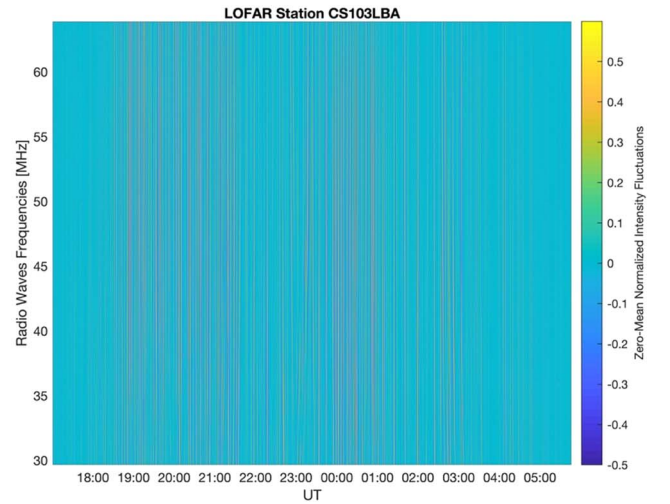
An example of this problem was provided in Fallows et al. (2014), where it is recognized that intensity fluctuations observed through KAIRA (McKay-Bukowski et al. 2015) originated from a single screen that was changing its distance and/or velocity during the integration time and not from multiple screens at different distances and with potentially different drift velocities (Fallows et al. 2014). The converse was demonstrated by Fallows et al. (2020), where the observed fluctuations were found to originate from two separate layers in the ionosphere.

In order to investigate this question, an example observation of the strong natural source Cassiopeia A (CasA, R.A. $23^{\text{h}}23^{\text{m}}24^{\text{s}}$, decl. $58^{\circ}48'54''$) taken between 17:01 UT on 2018 September 23 and 05:46 UT on 2018 September 24 is used. The data were taken under project LT10_001, with observation ID L668732. The one-dimensional power spectral density $\Phi_I(\nu)$ (at specific radio wave frequencies) and the two-dimensional power spectral density $P_I(t_d, f_D)$ were calculated for the intensity fluctuations observed from the LOFAR core station CS103, located near Exloo in the northeast of the Netherlands, over 200 subbands, each 195 kHz wide, covering the frequency range 29–64 MHz.

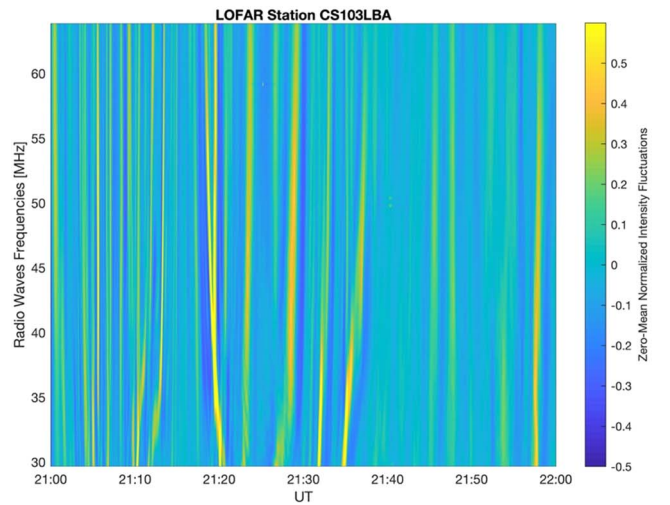
The intensity fluctuations were estimated as zero-mean normalized versions of the time series of the radio wave intensities received at each frequency. For this exercise the intensities were averaged in time from their original sampling interval, Δt , of 0.0105–0.9961 s, to make the data quantity more manageable. The analyses performed here do not suggest that a finer sampling rate is necessary for these ionospheric conditions. This is demonstrated by the fact that all the power spectral density is within temporal frequencies below 0.1 Hz (Figures 3–5).

For a radio wave with frequency $f = \frac{\omega}{2\pi}$, its received intensity $I(x_R, y_R, z_R, \omega, t)$ was normalized through a moving temporal average $\langle I(x_R, y_R, z_R, \omega, t) \rangle$ calculated over 180 points (i.e., approximately 3 minutes given the sampling interval $\Delta t = 0.9961$ s) as

$$\frac{I(x_R, y_R, z_R, \omega, t)}{\langle I(x_R, y_R, z_R, \omega, t) \rangle} \quad (17)$$



(a)



(b)

Figure 2. (a) Zero-mean normalized intensity fluctuations observed through LOFAR CS103 for all radio waves frequencies collected between 17:01 UT on 2018 September 23 and 05:46 UT on 2018 September 24. (b) Zero-mean normalized intensity fluctuations observed through LOFAR CS103 for all radio wave frequencies collected between 21:00 and 22:00 UT on 2018 September 23. Figure 2(b) is an enlarged section of Figure 2(a), showing only measurements between 21:00 and 22:00 UT from Figure 2(a).

The normalization in Equation (17) is helpful because the intensities of different radio wave frequencies f may have a trend and may show different dynamic ranges. Therefore, in order to establish a comparison across frequencies, relative changes through Equation (17) were considered.

The zero-mean normalized intensity fluctuations are given by

$$\begin{aligned} I_f(t) &= \frac{I(x_R, y_R, z_R, \omega, t)}{\langle I(x_R, y_R, z_R, \omega, t) \rangle} - \left\langle \frac{I(x_R, y_R, z_R, \omega, t)}{\langle I(x_R, y_R, z_R, \omega, t) \rangle} \right\rangle \\ &= \frac{I(x_R, y_R, z_R, \omega, t)}{\langle I(x_R, y_R, z_R, \omega, t) \rangle} - 1 \end{aligned} \quad (18)$$

and are illustrated in Figure 2. Overall, the normalization in Equation (18) attenuates the lowest spectral frequencies (e.g.,

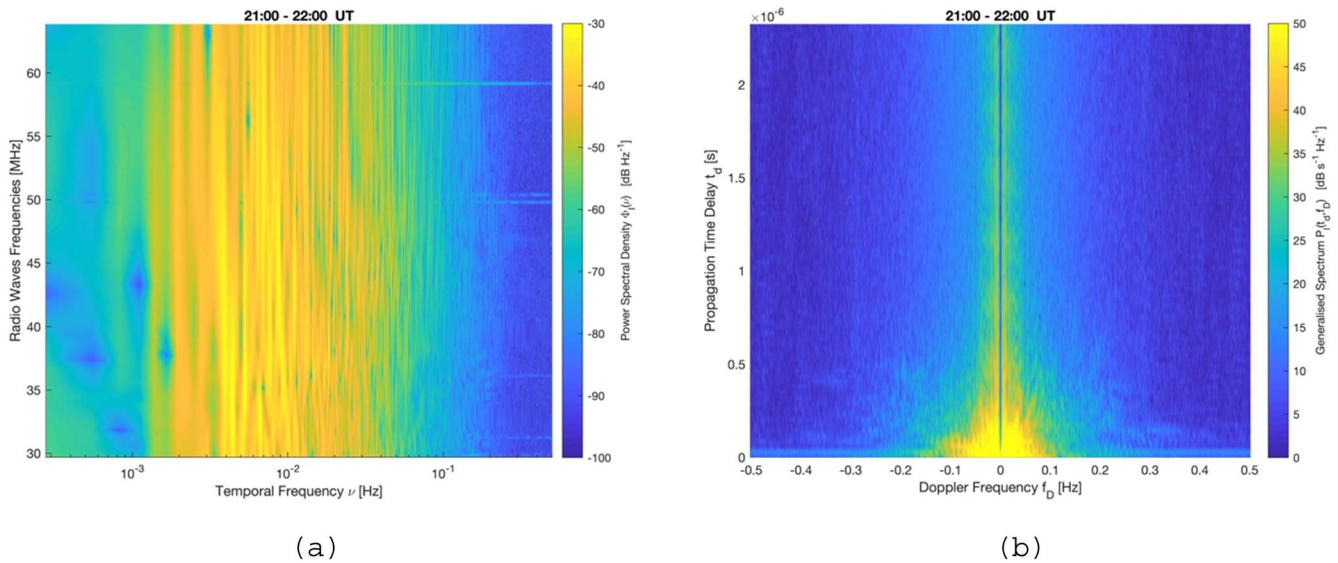


Figure 3. (a) Power spectral density $\Phi_I(\nu)$ and (b) generalized spectrum $P_I(t_d, f_D)$ of zero-mean normalized intensity fluctuations estimated over a time interval of 60 minutes between 21:00 and 22:00 UT on 2018 September 23.

those due to the apparent motion of the source); the use of a zero mean removes the zero-frequency (dc) spectral component.

The one-dimensional power spectrum $\Phi_I(\nu)$ (rather than $\Phi_\chi(\nu)$ in view of Equation (11)) and the two-dimensional power spectrum $P_I(t_d, f_D)$ were calculated for the zero-mean normalized intensity fluctuations $I_f(t)$.

The spectra in Figures 3–5 consider a representative shorter measurement interval (between 21:00 and 22:00 UT on 2018 September 23) and illustrate the differences observed on $\Phi_I(\nu)$ and $P_I(t_d, f_D)$ when calculated over different time intervals. For example, Figure 3 contains $\Phi_I(\nu)$ and $P_I(t_d, f_D)$ calculated over 60 minutes; Figure 4 shows the spectra calculated every 30 minutes; Figure 5 shows the spectra every 10 minutes. Differences seem to become evident when comparing power spectra estimated over 60, 30, and 10 minutes.

$\Phi_I(\nu)$ and $P_I(t_d, f_D)$ show spectral broadening in the interval 21:00–21:20 UT typical of strong scintillation (e.g., from multiple scattering) where the power-law roll-off at higher temporal frequencies can be substituted by a steeper Gaussian roll-off (Booker & Majidihi 1981; Basler et al. 1988; Knepp & Nickisch 2009). On the other hand, weak scattering with a more prominent Fresnel filtering (Equation (4)) seems to occur in the interval 21:40–22:00 UT. Overall, the observed radio wave frequencies experience weak-to-strong scattering with the scattering level not necessarily decreasing with the radio wave frequency, as illustrated in Figures 5(a)–(f).

Figure 5 suggests that the 10-minute $\Phi_I(\nu)$ and $P_I(t_d, f_D)$ modify their shape in response to different scattering regimes that vary with time. Such a change cannot be appreciated for the 60-minute spectra, while some modifications can be appreciated in the 30-minute spectra. The shape of $\Phi_I(\nu)$ (e.g., in the case of the radio wave frequency 45.1111 MHz) changes over consecutive 10-minute intervals between 21:00 and 22:00 UT in response to different scattering regimes, with spectral broadening occurring between 21:00 and 21:20 UT and more typical power-law roll-off occurring between 21:40 and 22:00 UT (Figure 5(m)).

Several features (i.e., symmetric and asymmetric arcs) can be observed in the 10-minute $P_I(t_d, f_D)$ in response to

different scattering regimes, while the 30- and 60-minute $P_I(t_d, f_D)$ appear to be the superposition of all the spectral features noticeable in the 10-minute $P_I(t_d, f_D)$ (similar examples of this aspect can be found in the estimates of $\Phi_I(\nu)$ and/or $P_I(t_d, f_D)$ contained in Hill et al. (2003), Stinebring (2006), Fallows et al. (2014), Bhat et al. (2016), Stinebring et al. (2019), Main et al. (2020), Reardon et al. (2020), and Liu et al. (2021)). The spread in delay and in Doppler is greater and asymmetric in the presence of strong scattering, whereas it reduces in the presence of weak scattering in analogy to $\Phi_I(\nu)$ (Figure 5).

Although the low-pass filtering introduced by the source filtering function varies with time and geometry (Yamauchi et al. 1996; Bisoi et al. 2014), such a variation occurs over time intervals much longer than the time interval considered in Figures 3–5 (de Gasperin et al. 2020). Therefore, the variation of the CasA source function is assumed to be negligible in the context of the spectral features of intensity fluctuations discussed within Figures 3–5.

An important indication from Figures 3–5 is that the longer the time interval considered, the less likely it is that the intensity fluctuations are ergodic. While the theoretical treatment described above relies on the assumption of homogenous stationary random functions, the experimental measurements reveal that the intensity fluctuations cannot be considered, in general, as stationary random functions. This introduces a limitation in the understanding of the properties of the propagation medium.

The different distribution of spectral energy over different temporal scales can be characterized by means of the continuous wavelet transform (CWT; Debnath & Shah 2010). The advantage of the CWT is that the contribution from different temporal scales can be appreciated without invoking ergodicity. An application of the use of a wavelet transform in the analysis of intensity fluctuations observed through the Solar-Terrestrial Environment Laboratory single-antenna radio telescope can be found in Aguilar-Rodriguez et al. (2014), where a wavelet transform was utilized for the estimate of the scintillation index, as well as the power law in $\Phi_I(\nu)$ (Aguilar-Rodriguez et al. 2014).

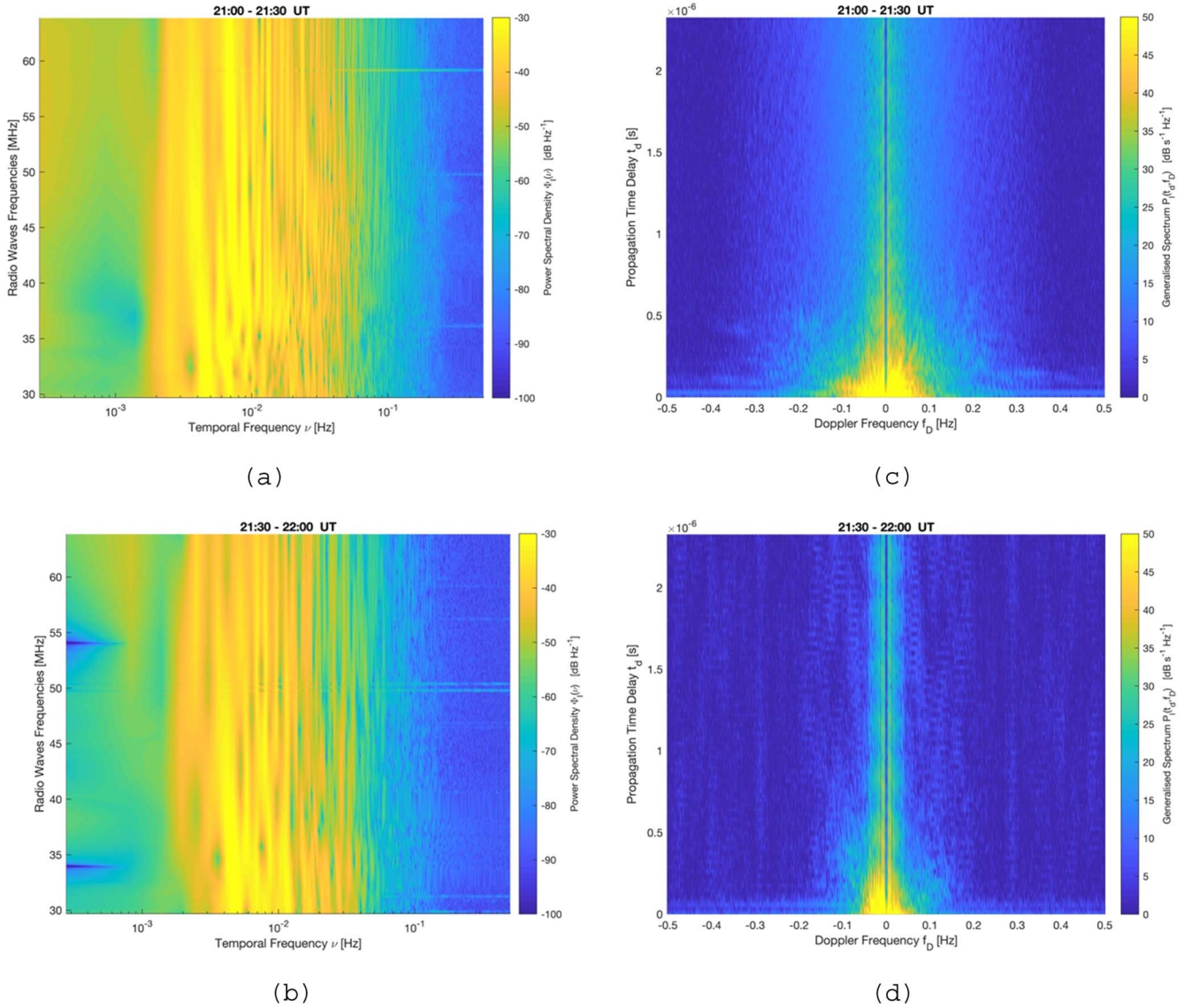


Figure 4. (a), (b) Power spectral density $\Phi_I(\nu)$ and (c), (d) generalized spectrum $P_I(t_D, f_D)$ of zero-mean normalized intensity fluctuations estimated over time intervals of 30 minutes. The intensity fluctuations were collected through LOFAR CS103 for radio wave frequencies in the range 29–64 MHz and refer to the same measurements as in Figure 3, between 21:00 and 22:00 UT on 2018 September 23.

Here the one-dimensional CWT was calculated for zero-mean normalized intensity fluctuations $I_f(t)$. The CWT was calculated by utilizing the MATLAB algorithm *cwt* based on the complex-valued Morlet wavelet $\Psi(t)$ as the mother wavelet (Debnath & Shah 2010):

$$\Psi(t) = e^{j\omega t - \frac{t^2}{2}}. \quad (19)$$

The CWT is based on a set of complex-valued functions that are translations and dilations of $\Psi(t)$, defined as (Debnath & Shah 2010)

$$\Psi_{\nu, \tau}(t) = \frac{1}{\sqrt{\nu}} \Psi\left(\frac{t - \tau}{\nu}\right) \quad (20)$$

and forming the basis of the CWT. The Morlet wavelet was chosen as the mother wavelet because it resembles the fluctuations typical of the radio wave intensity in the presence of scintillation. In the case of LOFAR multifrequency observations, the complex-valued one-dimensional CWT

$w_f(\nu, \tau)$ can be calculated for each zero-mean normalized intensity with frequency f , $I_f(t)$, as (Debnath & Shah 2010)

$$w_f(\nu, \tau) = \langle I_f(t) \Psi_{\nu, \tau}(t) \rangle = \int_{-\infty}^{+\infty} I_f(t) \Psi_{\nu, \tau}^*(t) dt, \quad (21)$$

where $\Psi_{\nu, \tau}^*(t)$ is the complex conjugate of $\Psi_{\nu, \tau}(t)$.

The LOFAR measurements are discrete, so that the time series of the received zero-mean normalized intensity fluctuations can be written as $I_{f_m}(t_k)$. Here f_m represents the values of the radio wave frequency (in hertz) observed through LOFAR. The corresponding discretized complex-valued CWT of $I_{f_m}(t_k)$ calculated through MATLAB can be written as $w_{f_m}(\nu_h, \tau_k)$, for each LOFAR radio wave frequency $29 \text{ MHz} \lesssim f_m \lesssim 64 \text{ MHz}$. The set of discrete values $w_{f_m}(\nu_h, \tau_k)$ are also known as the CWT coefficients (Debnath & Shah 2010). The CWT coefficients can be viewed as similar to the output of the discrete Fourier transform and can be appreciated in Figure 6 for $f_m = 29.6814 \text{ MHz}$ (Figure 6(a)) and $f_m = 63.8611 \text{ MHz}$ (Figure 6(b)). Figure 6 shows the absolute values of the CWT

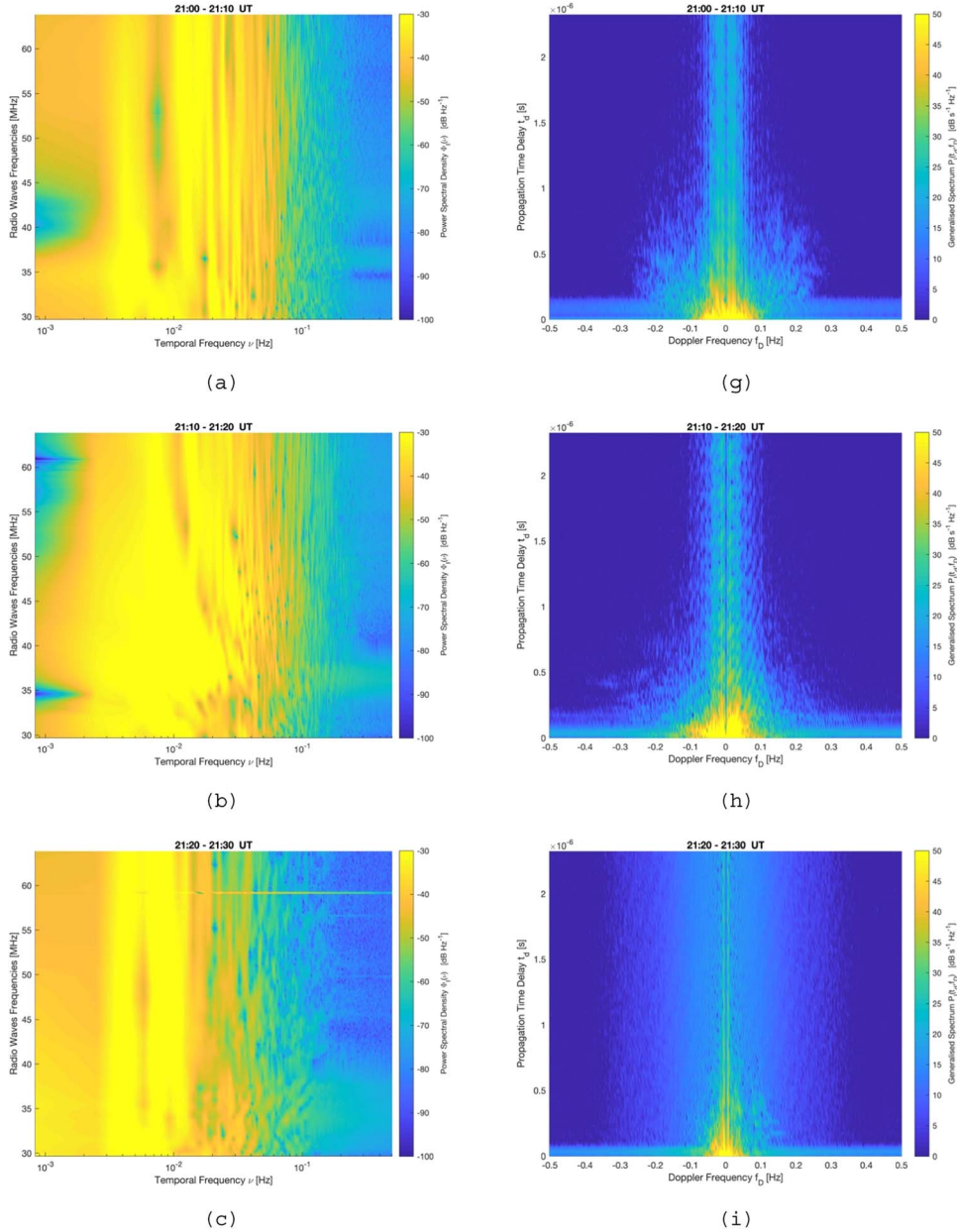


Figure 5. (a)–(f) Power spectral density $\Phi_I(\nu)$ and (g)–(i) generalized spectrum $P_I(t_d, f_D)$ of zero-mean normalized intensity fluctuations estimated over time intervals of 10 minutes. The intensity fluctuations were collected through LOFAR CS103 for radio wave frequencies in the range 29–64 MHz and refer to the same measurements in Figures 2–4, between 21:00 and 22:00 UT on 2018 September 23. The variation in the shape of $\Phi_I(\nu)$ for the radio wave frequency 45.1111 MHz is shown (panel (m)) over consecutive 10-minute intervals between 21:00 and 22:00 UT: 21:00–21:10 UT (black), 21:10–21:20 UT (red), 21:20–21:30 UT (green), 21:30–21:40 UT (cyan), 21:40–21:50 UT (blue), 21:50–22:00 UT (magenta). In panel (m), a moving average of the squared magnitude of $\Phi_I(\nu)$ is plotted via the MATLAB function *smooth* to improve visualization.

coefficients for the zero-mean normalized intensity fluctuations measured on specific radio wave frequencies received from CasA at LOFAR CS103 for the entire measurement between 17:01 UT on 2018 September 23 and 05:46 UT on 2018 September 24. The time interval considered is longer than that in Figure 5 to illustrate how multiple temporal scales can change over longer time intervals.

From Figure 6 it can be observed how the spectral energy is distributed over different temporal frequencies, localizing at different times irregularly and intermittently, thus suggesting instances of nonstationarity (Farge 1992; Debnath & Shah 2010).

An overview of the distribution of the spectral energy across the $\nu\tau$ plane is offered by the local intermittency parameter

(Farge 1992), defined as

$$L_{f_m}(\nu_h, \tau_k) = \frac{|w_{f_m}(\nu_h, \tau_k)|^2}{\langle |w_{f_m}(\nu_h, \tau_k)|^2 \rangle_{\tau_k}}, \quad (22)$$

where $\langle |w_{f_m}(\nu_h, \tau_k)|^2 \rangle_{\tau_k}$ is the average over an interval of time τ_k , which is denoted as T . Instances where $L_{f_m}(\nu_h, \tau_k) \neq 1$ indicate localization of the spectral energy, i.e., nonstationarity due, for example, to changes in the scattering regime (Farge 1992).

In order to appreciate how accurate the approximation of ergodicity can be, the variance of $L_{f_m}(\nu_h, \tau_k)$ over time τ_k at each spectral frequency ν_h and for each radio wave frequency 29 MHz $\lesssim f_m \lesssim$ 64 MHz is shown in Figure 7 over the same

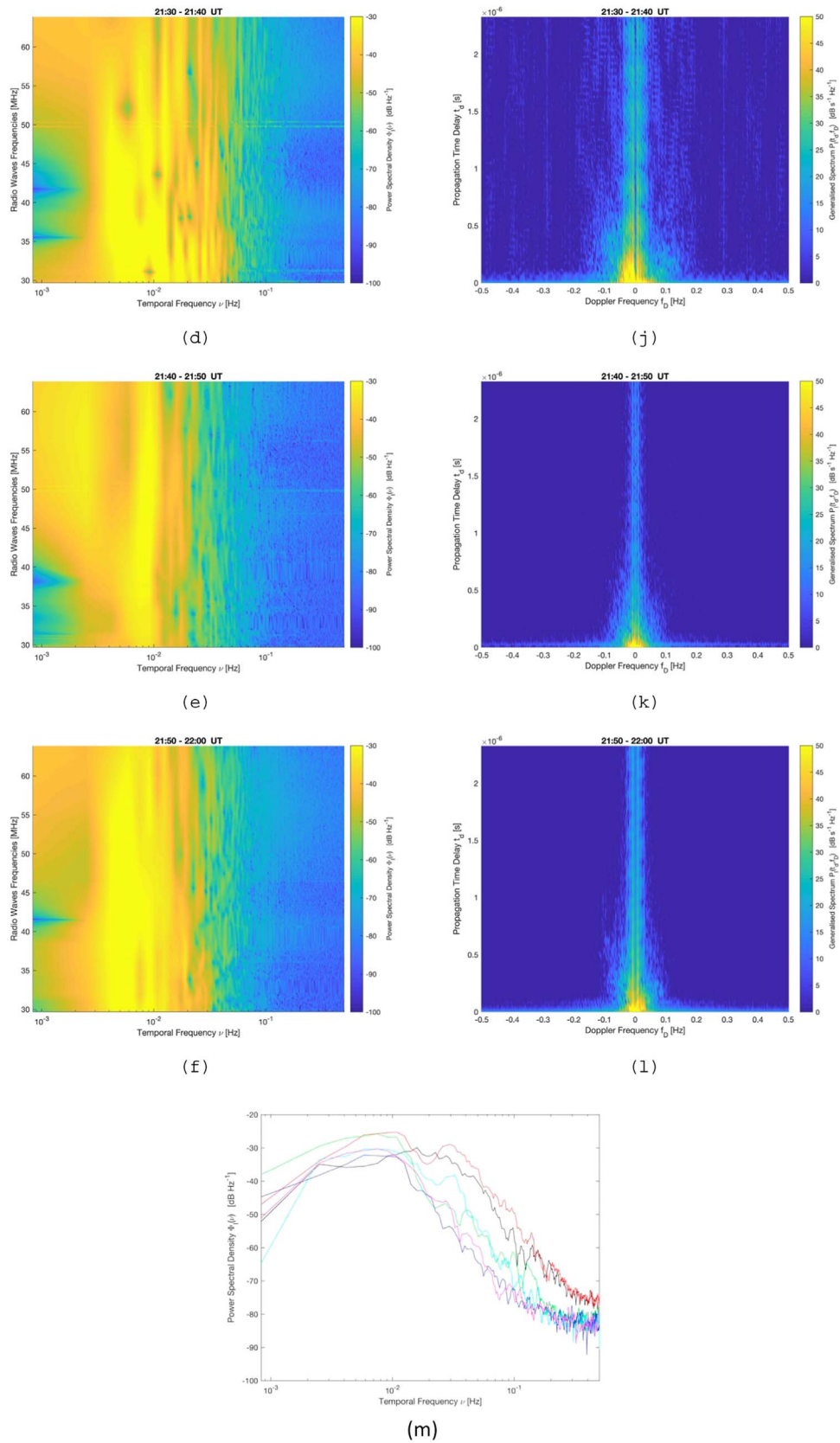


Figure 5. (Continued.)

time intervals (i.e., 60 minutes, 30 minutes, and 10 minutes) between 21:00 and 22:00 UT considered in Figures 3–5. The variance of $L_{f_m}(\nu_h, \tau_k)$ as a function of spectral frequency ν_h

was calculated with $L_{f_m}(\nu_h, \tau_k)$ averaged over the time interval $T = 60$ minutes (Figure 7(a), in analogy with Figure 3). The gray lines in Figure 7(a) refer to individual radio wave

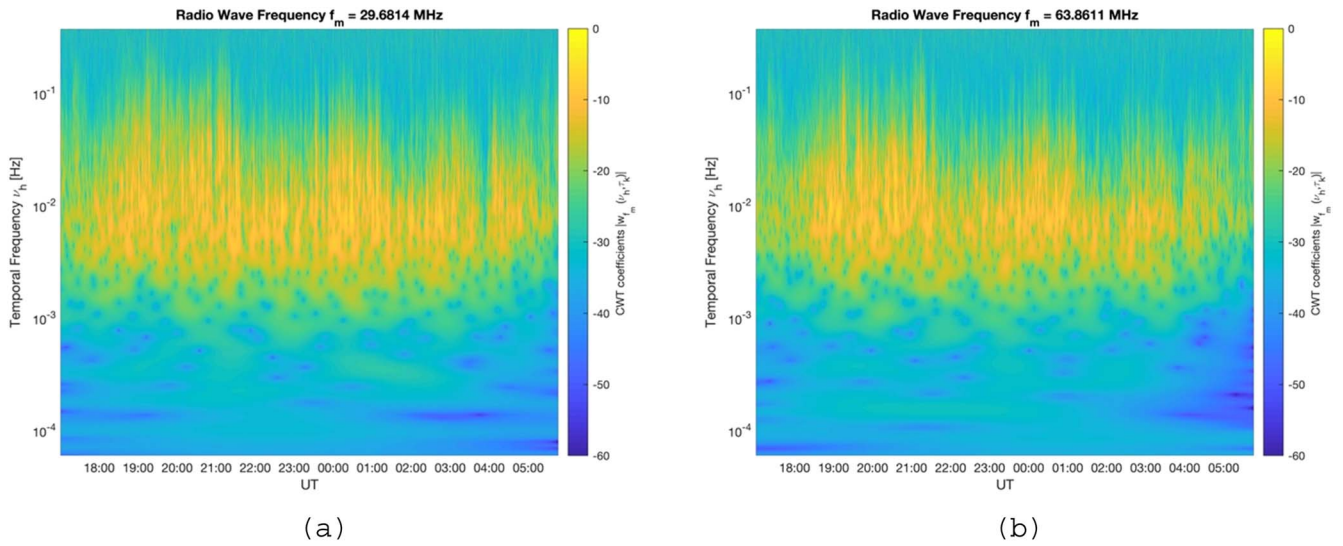


Figure 6. Absolute values of the CWT coefficients $|w_{f_m}(\nu_h, \tau_k)|$ in decibels for frequencies (a) $f_m = 29.6814$ MHz and (b) $f_m = 63.8611$ MHz. These are calculated for zero-mean normalized intensity fluctuations collected through LOFAR CS103 over the entire measurements' interval between 17:01 UT on 2018 September 23 and 05:46 UT on 2018 September 24.

frequencies f_m and the black line shows the average variance of $L_{f_m}(\nu_h, \tau_k)$ across all radio wave frequencies f_m over the time interval $T = 60$ minutes. A variance of zero would suggest a constant $L_{f_m}(\nu_h, \tau_k)$; in particular, if $L_{f_m}(\nu_h, \tau_k) \approx 1$, the spectral energy is not localized and the intensity fluctuations could be considered as ergodic to a fairly good approximation. However, the variance of $L_{f_m}(\nu_h, \tau_k)$ over 60 minutes between 21:00 and 22:00 UT for each radio wave frequency is not zero: it shows small values for 10^{-4} Hz $\lesssim \nu_h \lesssim 10^{-3}$ Hz, it tends to distribute around 1 for 10^{-3} Hz $\lesssim \nu_h \lesssim 10^{-2}$ Hz, and it shows large values for 10^{-2} Hz $\lesssim \nu_h \lesssim 10^0$ Hz (Figure 7(a)).

In Figure 7(b) $L_{f_m}(\nu_h, \tau_k)$ was averaged over the time interval $T = 30$ minutes, and only the average variance of $L_{f_m}(\nu_h, \tau_k)$ across all radio wave frequencies f_m is shown for simplicity: the black line refers to the interval 21:00–21:30 UT, and the red line refers to the interval 21:30–22:00 UT (in analogy with Figure 4). The variance of $L_{f_m}(\nu_h, \tau_k)$ for $\nu_h \gtrsim 10^{-1}$ Hz tends to be lower between 21:30 and 22:00 UT.

When $L_{f_m}(\nu_h, \tau_k)$ was averaged over the time interval $T = 10$ minutes, its variance (averaged across all radio wave frequencies f_m) appeared to attain lower values for 10^{-2} Hz $\lesssim \nu_h \lesssim 10^0$ Hz only in some of the 10-minute intervals considered between 21:00 and 22:00 UT (Figure 7(c), in analogy with Figure 5). This behavior is consistent with the varying scattering regime observed in Figure 5, that is, the alternation between weak scattering characterized by a spectral power-law roll-off (e.g., between 21:50 and 22:00 UT; Figure 5(f) and magenta line in Figure 7(c)) and strong scattering characterized by spectral broadening (e.g., between 21:10 and 21:20 UT; Figure 5(b) and red line in Figure 7(c)).

This point is further demonstrated in Figure 8, which shows the time variation of the local intermittency parameter $L_{f_m}(\nu_h, \tau_k)$ for each radio wave frequency f_m (gray lines) at three specific temporal frequencies. The time variation of $L_{f_m}(\nu_h, \tau_k)$ was evaluated between 21:10 and 21:20 UT (Figures 8(a)–(c), in relation to Figure 5(b) and red line in Figure 7(c)) and between 21:50 and 22:00 UT (Figures 8(d)–(f), in relation to Figure 5(f) and magenta line in Figure 7(c)). The

three temporal frequencies considered were $\nu_h = 0.0040847$ Hz (low-frequency end of the spectrum), $\nu_h = 0.024765$ Hz (central part of the spectrum where the Fresnel frequency can be located), and $\nu_h = 0.21234$ Hz (high-frequency end of the spectrum, where spectral broadening during strong scattering can occur). Figure 8 indicates that there are intervals shorter than 10 minutes where $L_{f_m}(\nu_h, \tau_k)$ has low values and low variance. The large values and large variance of $L_{f_m}(\nu_h, \tau_k)$ at the high-frequency end of the spectrum between 21:10 and 21:20 UT are consistent with the presence of spectral broadening due to strong scattering (see Figures 5(b) and 2(b)). The low values and low variance of $L_{f_m}(\nu_h, \tau_k)$ throughout the spectrum between 21:50 and 22:00 UT are consistent with the presence of weak scattering (see Figures 5(f) and 2(b)), except for some larger values toward the end of that interval where the ergodicity assumption is harder to sustain.

The analysis in Figures 7 and 8 indicates that the ergodicity assumption is not justified in the presence of strong scattering (e.g., between 21:10 and 21:20 UT), as $L_{f_m}(\nu_h, \tau_k)$ shows localization of the spectral energy (i.e., relatively large values with large variance); therefore, the use of the weak scattering results in this case is dubious. On the other hand, the ergodicity assumption is plausible in the presence of weak scattering (e.g., between 21:50 and 21:55 UT), as $L_{f_m}(\nu_h, \tau_k)$ shows low values with low variance; therefore, the use of weak scattering results in this case is appropriate.

A close inspection of Figures 8(e)–(f) reveals that $L_{f_m}(\nu_h, \tau_k)$ shows low values with low variance mainly between 21:50 and 21:55 UT; thus, the estimate of the Fresnel frequency on the basis of the weak scattering results is more appropriate over this 5-minute interval (or shorter intervals) rather than over the 10-minute interval between 21:50 and 22:00 UT. The calculation of $\Phi_I(\nu)$ and $P_I(t_d, f_D)$ was not attempted over shorter time intervals (e.g., over 5 minutes or shorter intervals between 21:50 and 21:55 UT) because the frequency resolution would start to become compromised in this case.

In order to carry out precise estimates of the Fresnel frequency in similar single-station observations, it is envisaged that $\Phi_I(\nu)$ and $P_I(t_d, f_D)$ are utilized in conjunction with the

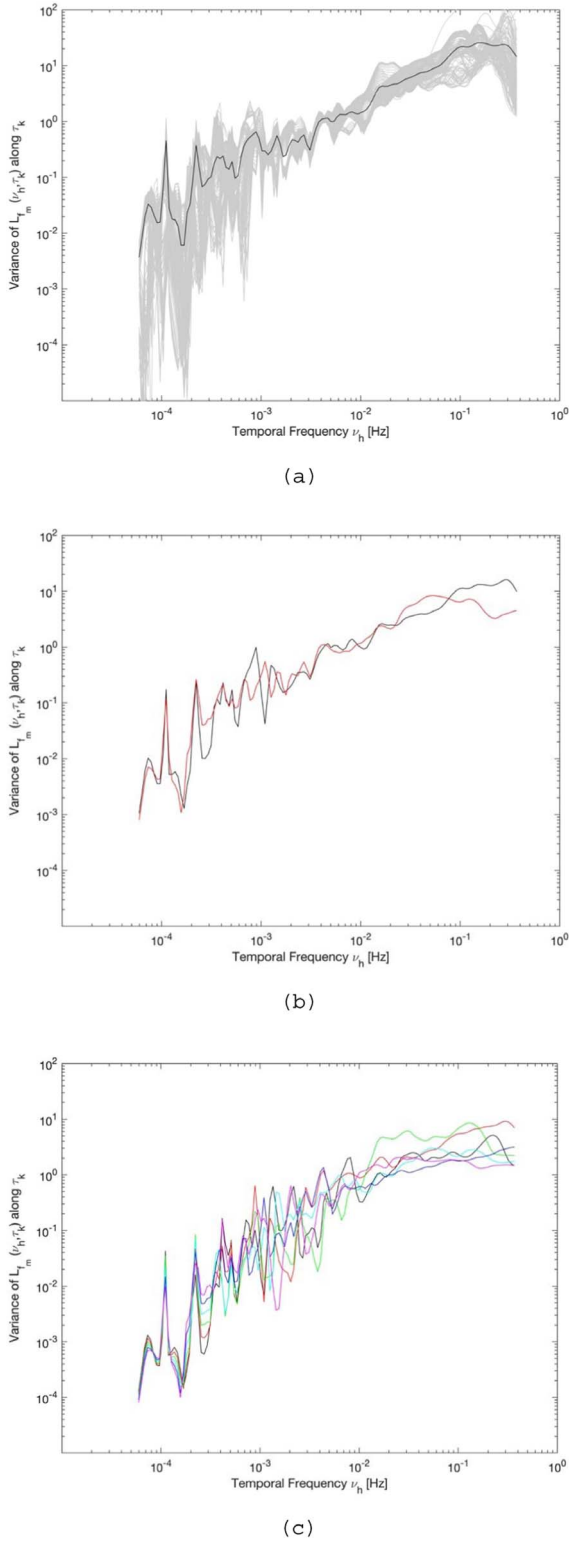


Figure 7. Local intermittency and its variance for the measurements collected between 21:00 and 22:00 UT on 2018 September 23. (a) The variance of $L_{f_m}(\nu_h, \tau_k)$ averaged over $T = 60$ minutes as a function of temporal frequency ν_h for each individual radio wave frequency f_m (gray lines) and its average across all radio wave frequencies f_m (black line). (b) The variance of $L_{f_m}(\nu_h, \tau_k)$ averaged over $T = 30$ minutes and across all radio wave frequencies f_m as a function of temporal frequency ν_h between 21:00 and 21:30 UT (black line) and between 21:30 and 22:00 UT (red line). (c) The variance of $L_{f_m}(\nu_h, \tau_k)$ averaged over $T = 10$ minutes and across all radio wave frequencies f_m as a function of temporal frequency ν_h in the intervals 21:00–21:10 UT (black line), 21:10–21:20 UT (red line), 21:20–21:30 UT (green line), 21:30–21:40 UT (cyan line), 21:40–21:50 UT (blue line), and 21:50–22:00 UT (magenta line).

local intermittency $L_{f_m}(\nu_h, \tau_k)$ to ascertain the presence of weak scattering, as well as the validity of the ergodicity assumption.

4. Origin of the Intensity Scintillation Observed

In order to investigate the second question (i.e., whether it is possible to distinguish, within data recorded by a single station and assuming a sufficiently compact source, between ionospheric, interplanetary, and interstellar scintillation), it is necessary to distinguish between weak and strong scattering. In the presence of weak scattering the functional form of $\Phi_I(\nu)$ can be utilized to infer $\Phi_{\Delta N}(\kappa_x, \kappa_y, 0)$, as well as the outer and inner scales of the inertial subrange. Furthermore, in the presence of weak scattering, Equation (8) can be utilized to estimate the distance to the phase screen (z_R) or the relative velocity between the ray path and the screen (V^{REL}) from the values of the Fresnel frequency (ν_F) that can be measured from the power spectrum $\Phi_I(\nu)$. Although the Fresnel frequency ν_F depends on both the distance z_R and the velocity V^{REL} , typically the distance z_R is assumed and Equation (8) is then solved for the velocity V^{REL} .

In the case of a phase screen in the solar wind or in the ionosphere and assuming that the velocities of the source and receiver are zero, V^{REL} can have, in principle, contributions from the drift of the irregularities in the solar wind V^{SW} ; the drift of the irregularities in Earth’s ionosphere V^{IONO} ; the rotation of Earth V^{ROT} , and the orbital velocity of Earth along the ecliptic plane V^{EARTH} . Typical values for these quantities are $V^{\text{EARTH}} \approx 30 \text{ km s}^{-1}$, $V^{\text{ROT}} \approx 465 \text{ m s}^{-1}$ (at the equator), $V^{\text{SW}} \lesssim 800 \text{ km s}^{-1}$, and $V^{\text{IONO}} \lesssim 1 \text{ km s}^{-1}$. Hence, the dominant contribution to V^{REL} in the case of a phase screen only in the interplanetary medium is V^{SW} , while the dominant contribution to V^{REL} in the case of a phase screen only in the ionosphere is V^{IONO} (as the ionosphere corotates with Earth). Various values of the Fresnel frequency according to Equation (8) due to the possible combinations of z_R and V^{REL} for various radio wave frequencies can be observed in Figure 9.

Figure 9 shows that for a phase screen at a fixed distance z_R from the receiver, the Fresnel frequency increases with the relative drift velocity V^{REL} . Conversely, for a fixed V^{REL} the Fresnel frequency decreases with increasing distance z_R . This is a consequence of the frozen-in assumption in conjunction with Equation (8).

Furthermore, different Fresnel frequencies can be observed for a phase screen at different distances from a receiver on Earth (and therefore different z_R) and for different relative velocities V^{REL} . A phase screen in Earth’s ionosphere ($100 \text{ km} \lesssim z_R \lesssim 1000 \text{ km}$) with a relative velocity $100 \text{ m s}^{-1} \lesssim V^{\text{REL}} \lesssim 1000 \text{ m s}^{-1}$ originates from Fresnel frequencies similar to a phase screen in the solar wind ($z_R \approx 1 \text{ au}$) with a relative velocity $100 \text{ km s}^{-1} \lesssim V^{\text{REL}} \lesssim 800 \text{ km s}^{-1}$.

The single LOFAR station considered here (CS103) is located at magnetic midlatitudes, and scintillation on the radio wave frequencies $29 \text{ MHz} \lesssim f_m \lesssim 64 \text{ MHz}$ considered in Figures 2–5 can arise from ionospheric irregularities forming in the presence of traveling ionospheric disturbances (TIDs; e.g., Kelley 2009; Fallows et al. 2020). TIDs can propagate with velocities approximately between 100 and 1000 m s^{-1} , and smaller-scale irregularities can form in the midlatitude ionosphere following a Perkins instability mechanism (Kelley 2009).

The data utilized here had a sampling interval of $\Delta t = 0.9961 \text{ s}$, leading to a Nyquist frequency of 0.54 Hz . In order to

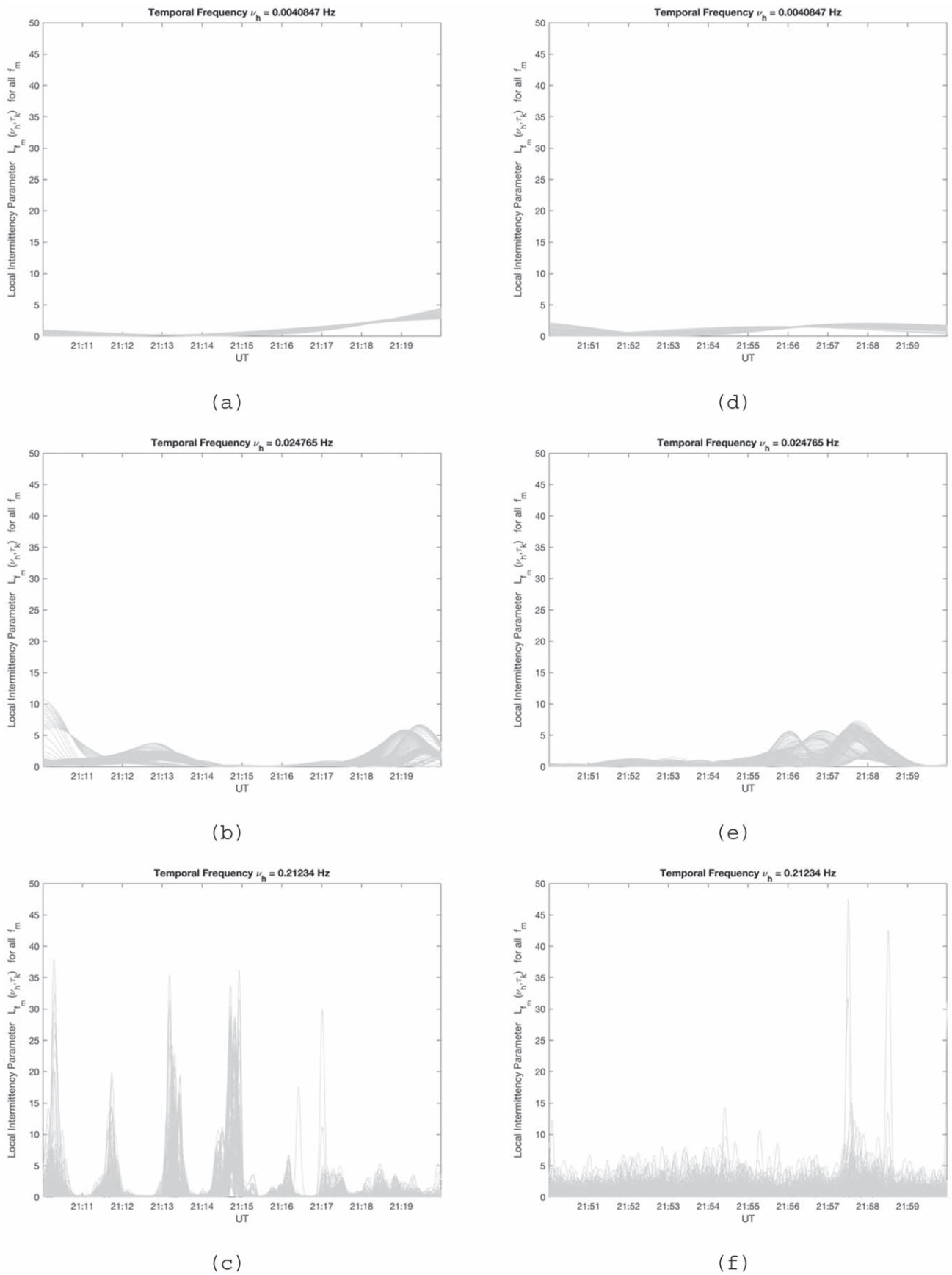


Figure 8. Time variation of the local intermittency parameter $L_{f_m}(\nu_h, \tau_k)$ for each radio wave frequency f_m (gray lines) at three temporal frequencies: $\nu_h = 0.0040847$ Hz, $\nu_h = 0.024765$ Hz, and $\nu_h = 0.21234$ Hz. (a)–(c) Strong scattering between 21:10 and 21:20 UT; (d)–(f) weak scattering between 21:50 and 22:00 UT.

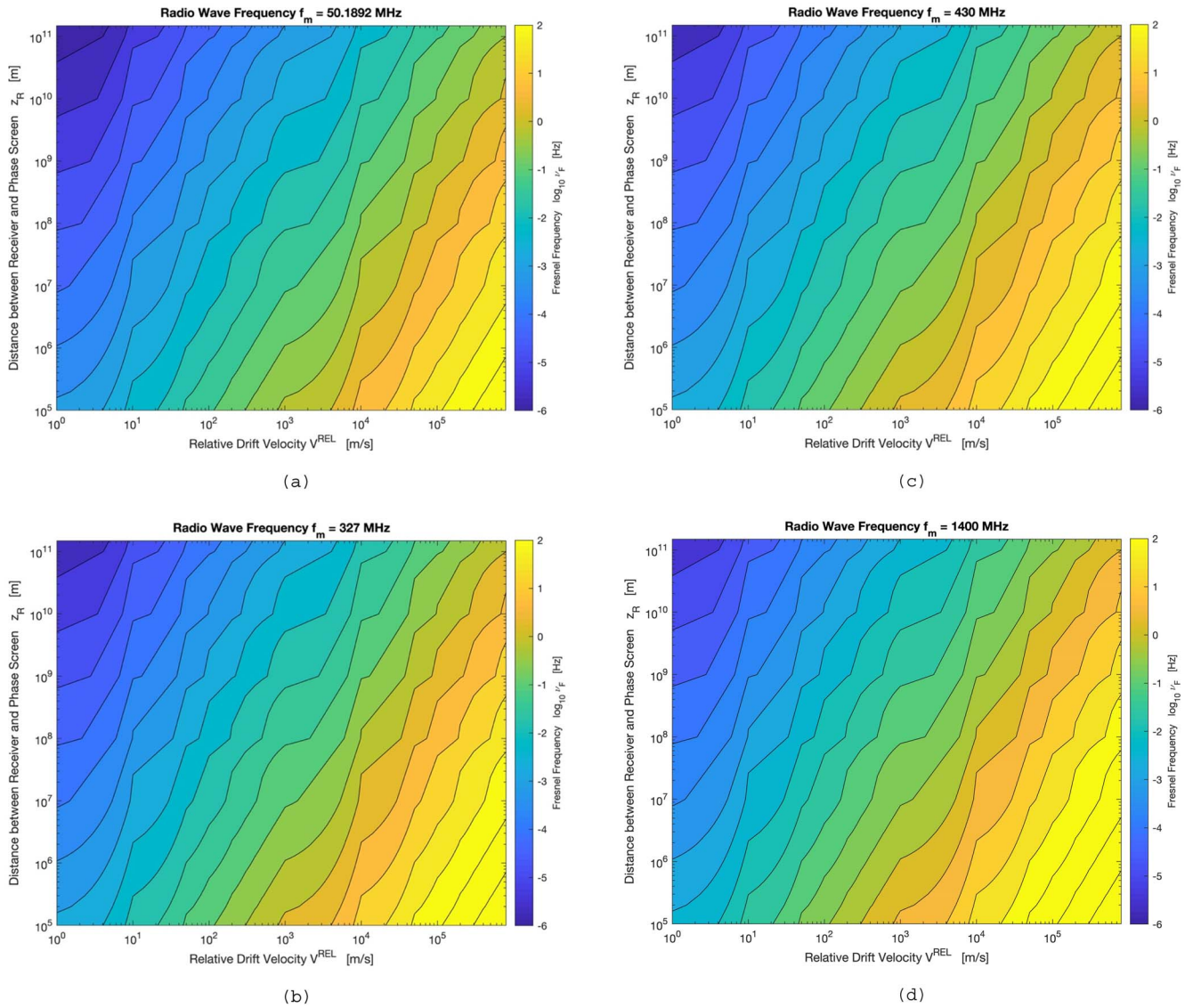


Figure 9. Fresnel frequencies ν_F calculated for combinations of different radio wave frequencies, phase screen distances z_R , and relative drift velocities V^{REL} on the assumption of weak scattering. (a) $f_m = 50.1892$ MHz, a representative LOFAR low-band frequency; (b) $f_m = 327$ MHz, a radio astronomy frequency typically used for observations of IPS; (c) $f_m = 430$ MHz, formerly observed, for example, with the Arecibo radio telescope; (d) $f_m = 1400$ MHz, a radio astronomy frequency typically used in the observation of pulsars.

detect intensity fluctuations arising from any screen located at $z_R > 1$ au or $z_R < 1$ au and with a relative velocity $V^{\text{REL}} > 800 \text{ km s}^{-1}$, a higher temporal resolution would be necessary. Sampling with a Nyquist frequency of at least 25 Hz is typical for observations of interplanetary scintillation (IPS).

The results of the weak scattering approximation for LOFAR radio frequencies $29 \text{ MHz} \lesssim f_m \lesssim 64 \text{ MHz}$ (Figure 9) suggest that the same Fresnel frequency of the order of 10^{-3} to 10^{-2} Hz can originate from a phase screen in the ionosphere, where $z_R \approx 300 \text{ km}$ and $V^{\text{REL}} \approx 100 \text{ m s}^{-1}$ (e.g., typical of medium-to-small-scale TIDs at midlatitudes and of inhomogeneous particle precipitation in the auroral ionosphere; Kelley 2009), as well as, in principle, from a phase screen in the solar wind, where $z_R \gtrsim 1 \text{ au}$ and $V^{\text{REL}} \gtrsim 200 \text{ km s}^{-1}$ (Manoharan & Ananthakrishnan 1990). Incidentally, pulsar observations with radio wave frequencies up to approximately 430 MHz fall in the 10^{-3} to 10^{-2} Hz interval (Hewish et al. 1985; Hill et al. 2003, 2005; Cordes et al. 2006).

Similarly, the same Fresnel frequency of the order of 10^{-2} to 10^0 Hz can originate from a phase screen in the ionosphere with high V^{REL} , where $z_R \approx 300 \text{ km}$ and $V^{\text{REL}} \approx 1000 \text{ m s}^{-1}$ (e.g., typical of large-to-medium-scale TIDs at midlatitudes; Kelley 2009), as well as from a phase screen in the solar wind, where $z_R \approx 1 \text{ au}$ and $V^{\text{REL}} \gtrsim 200 \text{ km s}^{-1}$ (Manoharan & Ananthakrishnan 1990). On the other hand, a Fresnel frequency of the order of 10^0 – 10^1 Hz can originate from a phase screen in the interplanetary medium where $z_R < 1 \text{ au}$ and $V^{\text{REL}} \gtrsim 200 \text{ km s}^{-1}$, typical of the solar wind (Manoharan & Ananthakrishnan 1990).

These ranges for Fresnel frequencies increase with the radio wave frequency as shown in Figure 9(b) for 327 MHz (i.e., the radio wave frequency observed at Ooty; Manoharan & Ananthakrishnan 1990), Figure 9(c) for 430 MHz, and Figure 9(d) for 1400 MHz (i.e., common radio frequencies observed in the case of pulsars; Cordes & Wolszczan 1986; Stinebring et al. 2001; Hill et al. 2003, 2005).

In the case of the single-station LOFAR observations considered here, there are two main aspects to consider when utilizing the results of the weak scattering approximation to deduce the relative velocity V^{REL} from the Fresnel frequency estimated from the measured scintillation: (a) the time intervals over which the signal is reasonably ergodic and is characterized by weak scattering need to be identified (this can be done by using the results in Section 3), and (b) even in the presence of low $L_{f_m}(\nu_h, \tau_k)$ with low variability and of weak scattering, there is ambiguity for a Fresnel frequency occurring in the interval $10^{-3} \text{ Hz} \lesssim \nu_h \lesssim 10^0 \text{ Hz}$, that is, whether the relative velocity V^{REL} is that of a phase screen in the interplanetary medium or in Earth's ionosphere.

For example, in the case of single-station LOFAR radio frequencies used here, $29 \text{ MHz} \lesssim f_m \lesssim 64 \text{ MHz}$, strong scintillation could be caused by irregularities in the interplanetary medium, as well as in Earth's ionosphere at middle latitudes.

When attempting to estimate parameters of the phase screen (e.g., its drift velocity), it is important to distinguish between weak and strong scattering. As strong scattering induces spectral broadening on $\Phi_I(\nu)$ (Booker & Majidihi 1981) and on $P_I(t_d, f_D)$ (Basler et al. 1988; Knepp & Nickisch 2009), an erroneous estimate for the Fresnel frequency could be made if this effect is not accounted for and separated from other effects (e.g., elongation of the source, extension of the source). For example, if the concept of the Fresnel frequency is erroneously utilized in the presence of strong scattering (Figures 5(a)–(b)), a higher value of ν_F and a higher Doppler spread would be obtained, leading to an erroneous estimate for z_R or V^{REL} . Instances of this aspect can be found in drift velocity estimates and conclusions contained, for example, in Chashei et al. (2016), Kaplan et al. (2015), and Imamura et al. (2014), whereas a demonstration of this aspect was provided in Fallows et al. (2016) through a comparison between estimates of $\Phi_I(\nu)$ from single-station observations and cross-correlation functions from multiple-station observations.

In the presence of strong scattering the concept of Fresnel scale no longer applies because multiple scattering occurs in an extended medium rather than weak scattering from a single phase screen (Booker & Majidihi 1981). In this case, intensity fluctuations develop within a focal distance that decreases with increasing phase perturbations introduced at each scattering; beyond the focal distance the wave front becomes incoherent (Uscinski 1977). Estimates of cross-correlation functions from multiple-station observations offer a more accurate estimate of V^{REL} in the presence of strong scattering (Kojima et al. 2013; Fallows et al. 2016).

From Equation (8), the error in ν_F (i.e., $\delta\nu_F$) can be described in terms of the error in V^{REL} (i.e., δV^{REL}) and the error in z_R (i.e., δz_R) to the first-order approximation as

$$\delta\nu_F = \left| \frac{\partial\nu_F}{\partial V^{\text{REL}}} \right| \delta V^{\text{REL}} + \left| \frac{\partial\nu_F}{\partial z_R} \right| \delta z_R. \quad (23)$$

In terms of relative errors, it can be shown that

$$\frac{\delta\nu_F}{\nu_F} = \frac{\delta V^{\text{REL}}}{V^{\text{REL}}} + \frac{1}{2} \frac{\delta z_R}{z_R}. \quad (24)$$

For example, at a fixed distance z_R the relative error in the estimate of the Fresnel frequency ν_F is equal to the relative error in the estimate of the relative drift velocity V^{REL} . If a Fresnel frequency $\nu_F \approx 10^{-1} \text{ Hz}$ is inferred from Figure 5(b) in the presence of strong scattering instead of a value of

$\nu_F \approx 10^{-2} \text{ Hz}$ that can be inferred from Figure 5(e) in the presence of weak scattering, the relative error for V^{REL} can be of the order of 900%. The error in the V^{REL} estimate propagates into an error in the estimate of the spatial spectrum and scales of electron density irregularities.

Therefore, the recognition of different scattering regimes can be utilized to identify errors in the estimates of parameters such as V^{REL} . These errors can, in turn, be utilized to optimize models of the propagation medium (e.g., solar wind).

5. Conclusions

The distinction between weak and strong scattering occurring on radio waves propagating from astronomical radio sources to Earth, together with the verification that ergodicity can be a reasonable approximation over the time interval considered, is essential for a correct estimate of the properties of the propagation medium. In the presence of ergodicity and of weak scattering the same Fresnel frequency (and therefore Doppler spread) can originate from a phase screen in Earth's ionosphere with V^{REL} typical of the ionosphere (as in the case of large-to-medium-scale TIDs at midlatitudes), as well as from a phase screen at $z_R \gtrsim 1 \text{ au}$ and with V^{REL} typical of the solar wind. The same Fresnel frequency characterizing pulsar observations up to approximately 430 MHz can originate from a phase screen in Earth's ionosphere with low V^{REL} (e.g., small-scale TIDs in the midlatitude ionosphere).

Strong scattering needs to be properly recognized and separated from other effects in order to avoid misleading estimates of Fresnel frequency and of Doppler spread: indeed, the concept of Fresnel frequency in relation to a single phase screen does not apply in this case, as radio waves encounter multiple scattering. While due care is normally applied to measurements of scintillation to ensure that a weak scattering condition is fulfilled, this work offers further methods to verify that this is indeed the case.

At a fixed propagation distance z_R the relative error in the Fresnel frequency ν_F is the same as that on the relative velocity V^{REL} . This aspect can be utilized to characterize errors in the description of the medium (e.g., solar wind).

Although the interstellar medium was not considered, the concepts described here apply to that case as well, in relation to corresponding phase screen distances and relative velocities. A separate discussion on this case will be prepared in the future. Also, further analyses on the combination of observations from LOFAR (e.g., scintillation measurements, all-sky imaging) and Global Navigation Satellite Systems to identify ionospheric structures will be explored.

The work carried out by B.F. at the University of Bath was supported by the UK Natural Environment Research Council (grant no. NE/R009082/1 and grant no. NE/V002597/1).

M.M.B. was supported in part by the STFC In-House Research grant to the Space Physics and Operations Division at UKRI STFC RAL Space. R.A.F. and M.M.B. were partially supported by the LOFAR4SW project, funded by the European Community's Horizon 2020 Programme H2020 INFRADEV-2017-1 under grant agreement 777442.









A.K. and B.D. would like to thank the Ministry of Education and Science of Poland for granting funds for the Polish contribution to the International LOFAR Telescope (decision No. 2021/WK/2) and for maintenance of the LOFAR PL-612 Baldy (decision No. 59/E-383/SPUB/SP/2019.1).

H.R. would like to thank the Ministry of Education and Science of Poland for granting funds for the Polish contribution to the International LOFAR Telescope (decision No. 2021/WK/2) and for maintenance of the LOFAR PL610 Borówiec (decision 6/E-73/SPUB/SP/2019).

This paper is based on data obtained with the International LOFAR Telescope (ILT) under project code LT10_001, with observation ID L668732. The original data are available in the LOFAR long-term archive at <https://lta.lofar.eu/Lofar>. LOFAR (van Haarlem et al. 2013) is the Low Frequency Array designed and constructed by ASTRON. It has observing, data processing, and data storage facilities in several countries that are owned by various parties (each with their own funding sources) and that are collectively operated by the ILT foundation under a joint scientific policy. The ILT resources have benefited from the following recent major funding sources: CNRS-INSU, Observatoire de Paris and Université d'Orléans, France; BMBF, MIWF-NRW, MPG, Germany; Science Foundation Ireland (SFI), Department of Business, Enterprise and Innovation (DBEI), Ireland; NWO, The Netherlands; The Science and Technology Facilities Council, UK; Ministry of Science and Higher Education, Poland.

The authors are grateful to two anonymous reviewers who provided very helpful suggestions.

ORCID iDs

Biagio Forte  <https://orcid.org/0000-0003-1682-1930>
 Richard A. Fallows  <https://orcid.org/0000-0002-5186-8040>
 Mario M. Bisi  <https://orcid.org/0000-0001-6821-9576>
 Jinge Zhang  <https://orcid.org/0000-0001-8641-9627>
 Andrzej Krankowski  <https://orcid.org/0000-0003-2812-6222>
 Bartosz Dabrowski  <https://orcid.org/0000-0002-4705-7798>
 Hanna Rothkaehl  <https://orcid.org/0000-0002-2067-1982>
 Christian Vocks  <https://orcid.org/0000-0001-8583-8619>

References

- Aarons, J. 1982, *IEEEP*, 70, 360
 Aguilar-Rodriguez, E., Rodriguez-Martinez, M., Romero-Hernandez, E., et al. 2014, *GeoRL*, 41, 3331
 Alfonsi, L., Spogli, L., Pezzopane, M., et al. 2013, *JGRA*, 118, 4483
 Basler, R. P., Price, G. H., Tsunoda, R. T., & Wong, T. L. 1988, *RaSc*, 23, 569
 Basu, S., MacKenzie, E., & Basu, S. 1988, *RaSc*, 23, 363
 Bello, P. 1963, *IEEE Trans. Commun. Syst.*, 11, 360
 Bhat, N. D. R., Ord, S. M., Tremblay, S. E., McSweeney, S. J., & Tingay, S. J. 2016, *ApJ*, 818, 86
 Bisoi, S. K., Janardhan, P., Ingale, M., et al. 2014, *ApJ*, 795, 69
 Booker, H. G., & Majidihi, G. 1981, *JATP*, 43, 1199
 Briggs, B. H., & Parkin, I. A. 1963, *JATP*, 25, 339
 Budden, K. G., & Uscinski, B. J. 1970, *RSPSA*, 316, 315
 Chashei, I. V., Tyul'bashev, S. A., Shishov, V. I., & Subaev, I. A. 2016, *SpWea*, 14, 682
 Cherniak, I., Krankowski, A., & Zakharenkova, I. 2018, *GPS Solut.*, 22, 2018
 Cordes, J. M., Rickett, B. J., Stinebring, D. R., & Coles, W. A. 2006, *ApJ*, 637, 346
 Cordes, J. M., & Wolszczan, A. 1986, *ApJ*, 307, L27
 de Gasperin, F., Vink, J., McKean, J. P., et al. 2020, *A&A*, 635, A150
 Debnath, L., & Shah, F. A. 2010, *Wavelet Transforms and their Applications* (Boston, MA: Birkhäuser)
 Fallows, R., Bisi, M. M., Forte, B., et al. 2016, *ApJL*, 828, L7
 Fallows, R. A., Coles, W. A., McKay-Bukowski, D., et al. 2014, *JGRA*, 119, 10544
 Fallows, R. A., Forte, B., Astin, I., et al. 2020, *JSWSC*, 10, 10
 Farge, M. 1992, *AnRFM*, 24, 395
 Fremouw, E. J., Leadabrand, R. L., Livingston, R. C., et al. 1978, *RaSc*, 13, 167
 Hewish, A., Scott, P. F., & Wills, D. 1964, *Natur*, 203, 1214
 Hewish, A., Wolszczan, A., & Graham, D. A. 1985, *MNRAS*, 213, 167
 Hill, A. S., Stinebring, D. R., Asplund, C. T., et al. 2005, *ApJL*, 619, L171
 Hill, A. S., Stinebring, D. R., Bamor, H. A., Berwick, D. E., & Webber, A. B. 2003, *ApJ*, 599, 457
 Imamura, T., Tokumaru, M., Isobe, H., et al. 2014, *ApJ*, 788, 10
 Ishimaru, A. 1978, *Wave Propagation and Scattering in Random Media* (New York: Academic Press)
 Jiao, Y., Morton, Y. T., Taylor, S., & Pelgrum, W. 2013, *RaSc*, 48, 698
 Jokipii, J. R. 1973, *ARA&A*, 11, 1
 Kaplan, D. L., Tingay, S. J., Manoharan, P. K., et al. 2015, *ApJL*, 809, L12
 Kelley, M. C. 2009, *The Earth's Ionosphere: Plasma Physics and Electrodynamics* (2nd ed.; Oxford: Elsevier)
 Knepp, D. L. 1983, *IEEEP*, 71, 722
 Knepp, D. L., & Nickisch, L. J. 2009, *RaSc*, 44, RS0A09
 Kojima, M., Coles, W. A., Tokumaru, M., & Fujiki, K. 2013, *SoPh*, 283, 519
 Kotulak, K., Zakharenkova, I., Krankowski, A., et al. 2020, *RemS*, 2, 2634
 Lambert, H. C., & Rickett, B. J. 1999, *ApJ*, 517, 299
 Little, L. T., & Hewish, A. 1966, *MNRAS*, 134, 221
 Liu, L.-J., Peng, B., Yu, L., et al. 2021, *MNRAS*, 504, 5437
 Main, R. A., Sanidas, S. A., Antoniadis, J., et al. 2020, *MNRAS*, 499, 1468
 Manoharan, P. K., & Ananthakrishnan, S. 1990, *MNRAS*, 244, 691
 McKay-Bukowski, D., Vierinen, J., Virtanen, I. I., et al. 2015, *ITGRS*, 53, 1440
 Mercier, R. P. 1962, *PCPS*, 58, 382
 Nickisch, L. J. 1992, *RaSc*, 27, 9
 Ratcliffe, J. A. 1956, *RPPH*, 19, 188
 Reardon, D. J., Coles, W. A., Bailes, M., et al. 2020, *ApJ*, 904, 104
 Redhead, A. C. S. 1971, *MNRAS*, 155, 185
 Salpeter, E. E. 1967, *ApJ*, 147, 433
 Secan, J. A., Bussey, R. M., Fremouw, E. J., & Basu, S. 1997, *RaSc*, 32, 1567
 Skone, S., Knudsen, K., & De Jong, M. 2001, *PCEA*, 26, 613
 Stinebring, D. R. 2006, *ChJAS*, 6, 204
 Stinebring, D. R., McLaughlin, M. A., Cordes, J. M., et al. 2001, *ApJL*, 549, L97
 Stinebring, D. R., Rickett, B. J., & Ocker, S. K. 2019, *ApJ*, 870, 82
 Uscinski, B. J. 1977, *The Elements of Wave Propagation in Random Media* (New York: McGraw-Hill)
 van Haarlem, M. P., Wise, M. W., Gunst, A. W., et al. 2013, *A&A*, 556, A2
 Vats, H. O., Booker, H. G., & Majidihi, G. 1981, *JATP*, 43, 1235
 Walker, M. A., Melrose, D. B., Stinebring, D. R., & Zhang, C. M. 2004, *MNRAS*, 354, 43
 Yamauchi, Y., Kojima, M., Tokumaru, M., et al. 1996, *JGG*, 48, 1201
 Yeh, K. C., & Liu, C.-H. 1982, *IEEEP*, 70, 324
 Zakharenkova, I., Cherniak, I., & Krankowski, A. 2019, *JGRA*, 124, 10728